Lawrence Berkeley National Laboratory

Title

Mechanistic Advantages of Organotin Molecular EUV Photoresists

Permalink

https://escholarship.org/uc/item/3x90g591

Journal

ACS Applied Materials & Interfaces, 14(4)

ISSN

1944-8244

Authors

H., Jonathan
Needham, Craig
Wang, Han
et al.

Publication Date

2022-02-02

DOI

10.1021/acsami.1c12411

Peer reviewed

Mechanistic Advantages of Organotin Molecular EUV Photoresists

Jonathan H. Ma,*[†,‡] Craig Needham,[¶] Han Wang,[§] Andrew Neureuther,[†,‖] David Prendergast,[⊥] and Patrick Naulleau*[,†]

†Center of X-Ray Optics, Lawrence Berkeley National Lab, Berkeley, California 94720, USA

‡Department of Physics, University of California, Berkeley, California 94720, USA

¶Inpria Corporation, 1100 NE Circle Blvd. Suite 360, Corvallis, OR 97330, USA

§Chemical Sciences Division, Lawrence Berkeley National Laboratory, Berkeley, California 94720, USA

‖Department of EECS, University of California, Berkeley, California 94720, USA

⊥Molecular Foundry, Lawrence Berkeley National Laboratory, Berkeley, California 94720, USA

E-mail: jonathanma1000@berkeley.edu; pnaulleau@lbl.gov

Abstract

The Extreme Ultraviolet(EUV)-induced radiation exposure chemistry in organotin-oxo systems, represented by the archetypal $[(R-Sn)_{12}O_{14}(OH)_6](A)_2$ cage, has been investigated with density functional theory. Upholding existing experimental evidence of Sn-C cleavage dominant chemistry, computations have revealed either electron attachment or ionization can single-handedly trigger tin-carbon bond cleavage, partially explaining the current EUV sensitivity advantage of metal oxide systems. We have revealed that tin atoms at different parts of the molecule react differently to ionization and

electron attachment, and have identified such selectivity as a result of local coordination chemistry instead of the macro geometry of the molecule. An ionization–deprotonation pathway has also been identified to explain observed evolution of anion conjugate acid upon exposure and anion mass dependence in resist sensitivity.

Keywords

Lithography, EUV, Photoresist, Organotin compounds, Radiation chemistry, DFT

1 Introduction

Metal-organic systems have found a wide variety of applications[1–3] . In particular, organotin compounds have generated interest in certain applications, including catalysis,[4] atomic layer deposition and lithography.[5–7] Organotin compounds come in many forms[8] and the "football" cage, as shown in figure 1 (a), has demonstrated its potential for catalysis[4] and lithographic applications.[6] The introduction of EUV lithography gave rise to new demands and performance criteria for photoresists and organotin-oxo systems have become a leading contender.

Photoresists are thin films that convert an optical image into a mechanical mask.[9] Upon exposure to the optical image, chemical changes are induced in the exposed areas. These changes directly or indirectly lead to change in solubility. At this point, the optical image has been translated into latent solubility contrast. By rinsing the exposed film with appropriate agents, which are known as the developers, the exposed or unexposed regions can be selectively removed, leaving behind a mask that resembles the optical image. A good example is the workhorse chemically amplified resist (CAR). In these systems, photon absorption leads to the generation of an acid molecule. Afterwards the system is baked, allowing the acid to diffuse, catalytically (thus chemical amplification) convert non-polar protecting groups into polar moieties. As a result, the exposed area is more polar. Upon contact with a polar

developer, the exposed region is removed but the unexposed regions remain intact.

Currently, it is common for the above process to produce features that are only dozens of manometers in size. To push feature sizes even smaller, EUV lithography has been introduced, essentially to produce finer optical images. Resist materials therefore need to keep up and that immediately brought forth two related challenges.

Firstly, there is a trade off between resolution, line width roughness, and sensitivity, which is known as the RLS trade-off.[10] Each EUV photon carries an energy of 92 eV, which is more than 10 times of a deep ultraviolet (DUV) photon used prior to EUV. As a result, with the same power, the number of photons drop by a factor of more than 10, resulting in much noisier images that produce rougher lines, increasing the risk of electrical failure. To mitigate this problem, resolution or dose has to be sacrificed. However, giving up resolution defeats the point of introducing EUV and increasing dose undermines the cost effectiveness of EUV lithography. A workaround is needed and it appears that there are a few ways to combat this trade-off. One can look into alternative material platforms or try to increase the quantum efficiency, which is the average number of chemically active species generated by an absorbed photon.[10,11]

Secondly, while chemically active species are generated by photochemistry in DUV, in EUV they are created by a secondary electron cascade initiated by EUV photon ionization.[9,12] The cascade ultimately produces multiple radical cations and low energy electrons, both of which are responsible for chemistry. Taking CARs as an example, in DUV, acid generation is relatively well understood because it is driven by photochemistry. In EUV however, acid generation is still a subject of research and is hypothesized to involved very different pathways.[9,12] The drastic move from DUV photochemistry to EUV radiation chemistry opens the door for new materials that would potentially suit EUV better than CARs.

To address these two challenges, new materials have been explored. Organotin resists have shown potential for a few reasons. Firstly, tin atoms have a high EUV absorption cross-section,[13] thus facilitating better sensitivity. Using density data from Banse et. al.[14]

3

and X-ray cross-section data from the CXRO database,[15] the butyl variant of the "football" cage[14] has an X-ray absorption coefficient of $12.8 \mu m^{-1}$, which is much higher than $4.03 \mu m^{-1}$ of poly(hydorxystyrene), a proxy for polymeric CAR systems. Secondly, the carbon-tin bond is chemically stable in comparison with alkyl bonds to more conventional transition metals. Such bond strength allows for more stable manufacturing processes. Last but not the least, as we will illustrate in this work, both ionization and electron attachment trigger similar chemical responses, potentially providing higher quantum efficiency, putting us in a better position against the RLS trade-off.

Commercial metal oxide resists has already demonstrated industry leading resolution at sub 10-nm half pitch compared to CARs.[16–18] Moreover, it is better positioned than CAR resists in overcoming the RLS trade-off.[17] To understand the origin of its superiority and fully exploit the potential of these compounds for EUV applications, the exposure chemistry should be closely examined. Moreover, a more thorough mechanistic understanding could enable systematic improvements in quantum efficiency, thus equip us better against the RLS trade-off.[11] To that end, we expand on our previous endeavor[19] and use density functional theory to thoroughly examine the thermal chemistry subsequent to EUV exposure.

To gain insights, we employ the prototypical "football" $[(R-Sn)_{12}O_{14}(OH)_6](A)_2$ compound (which will be referred to as $\mathbf{Sn_{12}R_{12}(A)_2}$), which has been the center of mechanistic studies for organotin resist.[6,20–23] With proper process conditions, even this model organotin-oxo compound, a basic system used for research, is capable of achieving sensitivity comparable with commercial CAR systems in academic settings, indicating its potential for practical applications.[24]

Given that the chemistry is based upon tin-carbon bond cleavage taking place in a tin-oxo framework, insights gained from studying this system could be useful for understanding similar systems under investigation for application in EUV lithography, such as tin Keggin ions.[25–27]

As shown in figure 1, $\mathbf{Sn_{12}R_{12}(A)_2}$ consists of twelve tin atoms connected by oxo-bridges,

consistent with X-ray crystallography.[14] Six of the tin atoms sit on the "belt" and the other six reside on the "caps"—three for each cap. The tin atoms on the belt are five-coordinate and the ones on the caps are six-coordinate. Each tin atom is connected to an organic side group (R−). Similar molecular frameworks have been reported with different metals such as titanium $[(EtO-Ti)_{12}O_{14}(OEt)_4(O)_2](A)_2$[28] and vanadium $[(O-V)_{12}O_{12}F_2(OH)_6]^{6-}$.[29]

The tin cage has a charge of 2+, thus it is normally accompanied by two anions with charge 1−. Through substitution techniques, cages with various anions have been successfully separated and their properties have been investigated.[24,30] While the anion has been shown to have an effect on exposure sensitivity,[6,24] the anion is believed to play a secondary role to tin-carbon bond chemistry.[20,23] As we will demonstrate, the tin-carbon bond strength changes by less than 0.1 eV upon the removal of both anions. To simplify calculations, the hydroxide ion is used in this work. Multiple organic side groups have been synthesized and assessed in previous experimental endeavors.[31,32] To focus our attention on the radiation chemistry of the system, which centers around the tin-carbon bond, we start our investigation with methyl ligands

As previously mentioned, the biggest difference between EUV and and DUV lithography is the ionizing nature of EUV radiation excitation source. Due to its high energy, a single EUV photon leaves behind multiple pairs of ionized molecules and low energy electrons.[9,12] The prevalence of impact ionization and low energy electrons led to the understanding that these events, instead of UV-induced optical transitions, are responsible for initiating exposure chemistry that ultimately results in solubility switching.

Most previous studies used the $\mathbf{Sn}_{12}\mathbf{R}_{12}(A)_2$ "football" cluster as a "molecular resist" where all functionalities are packed into a single molecule[6,20–23] (x-ray crystallography has revealed residual solvent molecules[14]). In that case, both ionization and electron attachment occur in the cluster and the effects of these phenomena on bond strengths and stability have been sporadically explored[22] but are yet to be understood in a comprehensive manner. While experimental endeavors have resulted in a rather qualitative understanding of the exposure

chemistry, they can be complemented by quantitative investigations which interrogate the details of ionization and electron attachment induced processes.

2 Computation Methodology

We therefore investigate the network of relevant reactions with quantum chemistry. To strike a balance between throughput and accuracy, we would limit our investigation to the electronic ground state, which if unstable, is strong evidence for ionization or electron attachment driven chemistry. Due to the size of the system, the revised PBE0-D3(BJ) hybrid functional[33] was chosen. Considering that the system is ionic and the radical nature of ionized and electron-attached species, mitigating self-interaction error (SIE) is a priority in the choice of functional. The PBE family has been parameterized to minimize SIE[34] and was shown to perform well with radicals among common hybrid functionals.[35]

To incorporate dispersion interaction, D3 corrections[36] with BJ damping[37] is used. Non-local dispersion correction has been considered but the lack of analytic Hessian makes such implementations impractical.

Structures are relaxed with Ahlrich's def2-SVP basis set. The same basis set was used in Hessian calculations to extract vibrational modes and thermochemistry at room temperature. Those same Hessian calculations were used to confirm that imaginary modes (with the exception of methyl rotor modes) do not exist. To compute the electronic energy, we performed high accuracy single point calculations with the def2-TZVP basis set. In all calculations, the effective core potential def2-ECP was used for Sn atoms. All calculations were carried out with Q-Chem.[38]

Excited state chemistry could be at play. Radiation processes, in particular ionization, would often excite a molecule to an electronic excited state. However, to fully understand how chemistry is driven by electronic excited states in this context, multi-reference or wave-function methods are needed. Excited-state chemistry often leverages the potentially disso-

ciative potential energy surface (PES). In a bond-breaking process the single determinant description of the electronic structure often breaks down, rendering multi-reference methods such as complete active space self consistent field (CASSCF) necessary.[39] Such methods, albeit accurate, are impractical for $\mathbf{Sn}_{12}\mathbf{R}_{12}(A)_2$. A state-of-the-art CASSCF algorithm can efficiently compress the determinant space to enable an active space of (50,50).[40] However, in the simplest variant (R = methyl and A = none), $\mathbf{Sn}_{12}\mathbf{R}_{12}(A)_2$ comprises 86 atoms, which results in a frontier manifold of 88 occupied canonical orbitals. Such computations could still be possible after careful selection of the active space but they are, however, not practical as we set out to elucidate a network of reactions.

As excited state chemistry is excluded from this work, our investigation would provide an effective "lower bound" for reactivity—if cleavage happens at the electronic ground state, it likely happens at an excited state as well. Yet if no cleavage takes place at the electronic group state, cleavage at an excited state cannot be ruled out.

We will first have an overview of the thermochemical reaction network of a the prototypical tin-oxo cage upon single electron attachment or ionization, in the presence of two, one, and zero counter anions. By examining the network of reactions, we report a few intriguing phenomena.

3   Results and Discussions

3.1   Overview

The cage can be accompanied by zero, one, or two hydroxide ions. We first focus on the charge-neutral variant with both hydroxide anions, $\mathbf{Sn}_{12}\mathbf{Me}_{12}(OH)_2$ as shown in figure 1(a). As one can see there are two categories of tin atoms (and corresponding tin-carbon bonds)-—the ones near the cap (figure 1(b)) are 6-coordinate and those on the belt (figure 1(c)) are 5-coordinate. The counter anions are located at the caps in figure 1(d).

Prior to ionization or electron attachment, as shown in figure 2 the bond dissociation free
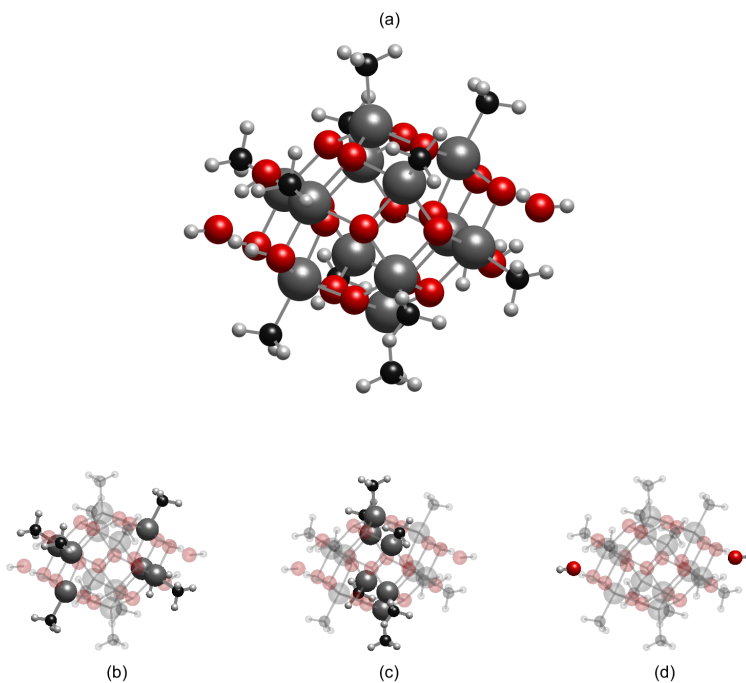
Figure 1: The structure of $\mathbf{Sn}_{12}\mathbf{Me}_{12}(OH)_2$ is shown in (a). Red, gray, black and white atoms are oxygen, tin, carbon and hydrogen, respectively. The cap and belt tin-carbon bonds are highlighted in (b) and (c) and the counter anions, in this case OH^-, are highlighted in (d)

energies (BDFE) are 2.47 and 2.43 eV for belt and cap methyl groups, which is consistent with thermal programmed desorption (TPD) measurements on a similar system (2.4 to 3.0 eV).[41] Our calculations were performed in gas phase. Compared to the condensed film used in the experiment, we anticipate the entropy gain from dissociation to be larger in vacuum, resulting in an underestimation of the BDFE. The slight preference for belt homolysis is consistent with previous computational study. The inclusion of entropy and dispersion energy reduces the difference from 0.1 eV to 0.04 eV.

Rather unsurprisingly, homolysis(removal of $CH_3 \cdot$) is significantly more favorable than heterolysis (removal of CH_3^+)—heterolysis BDFE are 8.7 and 9.5 for belt and cap methyl groups. The difference between the two is related to the geometry of the frontier orbitals. Heterolysis, in context, is homolysis followed by ionization of $CH_3^{\bullet}$ and electron addition to the de-methylated cage. As shown in figure 3, the highest occupied molecular orbital
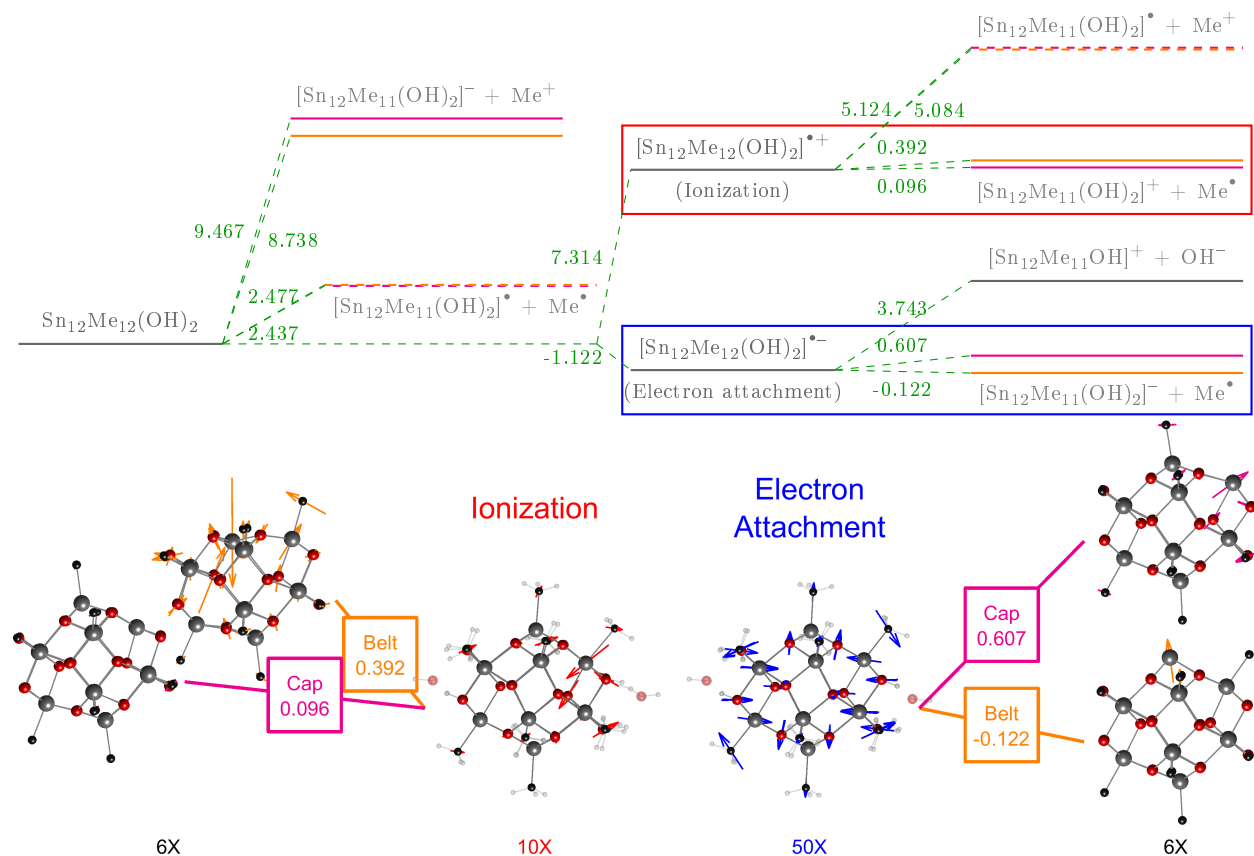
Figure 2: A graphical representation of reaction free energies for $\mathbf{Sn_{12}Me_{12}(OH)_2}$. Ionization, electron-attachment, and bond-dissociation reactions are included. Energy levels are drawn to scale. Numbers are reaction free energies in eV. Belt/cap methyl dissociation levels are in orange/magenta, respectively. The post-ionization and electron attachment demethylation reactions are expanded in the bottom left and right panels. Red/blue arrows in the insets indicates scaled atomic displacement from neutral equilibrium geometry upon ionization/electron attachment. Orange/magenta arrows indicate tin-oxo cage atomic displacement upon removal of belt/cap methyl groups from respective their perturbed (ionized or electron attached) geometries. Numbers at the bottom are magnifications for atomic displacements.

(HOMO, shown in figure 3 (b)) and the near degenerate HOMO-1 (shown in figure 3 (a)) is mostly a bonding orbital localized around the cap tin-carbon bonds. On the other hand, the lowest unoccupied molecular orbital (LUMO, shown in figure 3(c)) is localized around the belt tin atoms. As a result of heterolysis, the methyl-deficient cage has one electron more than it has after homolysis. No matter if this extra electron enters either the LUMO (SOMO without this extra electron) or the HOMO, it will preferentially stabilize the cap tin-carbon bonds.

3.2 One electron redox

As previously mentioned, chemistry is expected to be generated by ionization[22] and electron attachment upon EUV exposure[20] in this system and in EUV in general.[12] The low-energy electrons are known to result in dissociative electron attachment in certain systems. To investigate this possibility, we began with determining whether the electron affinity is positive. Our computation indicates that the adiabatic electron affinity is 1.1 eV, suggesting that electron attachment is favorable.

Upon one-electron ionization, the tin-carbon bonds are also destabilized. In this scenario, as one can see in the upper panel in figure 2, the cap tin-carbon bonds are weakened preferably. Although cleavage is not spontaneous after including the entropy gain at room temperature, the BDFE is on the order of 0.1 eV, which is surprisingly lower than previously reported. We attribute the difference to the inclusion of entropy, enthalpy, and dispersion interaction. The reaction entropy contribution (TΔS) is 0.45 eV for the cap methyl group and 0.67 eV for the belt methyl group. Inclusion of counter anions, as we will demonstrate later on, does not explain the difference. There is an apparent discrepancy between our BDFE and multi-reference bond strength[39] (0.09 vs 0.96 eV) but they are not directly comparable as the multi-reference calculation only provides the electronic contribution. By ignoring the vibrational (zero point and finite temperature) and entropic contributions to the BDFE, the PBE0-D3(BJ) contribution to this reaction is 0.67 eV.
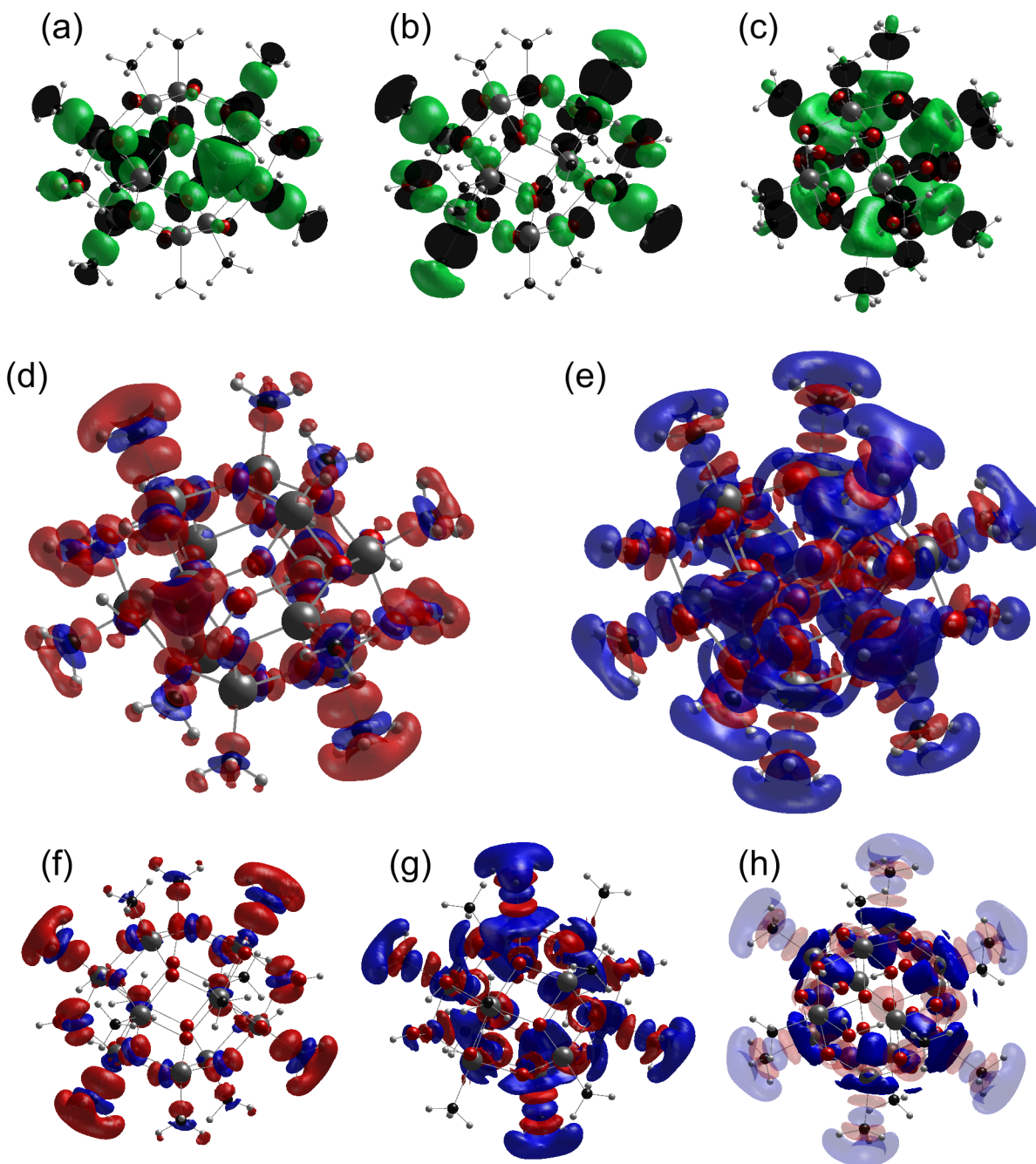
Figure 3: (a-c) HOMO-1, HOMO, and LUMO iso-surfaces taken at values ± 5.48e-2Å$^{-1.5}$. Color indicates sign. (d,e) The iso-surfaces of electron density change when $\mathbf{Sn}_{12}\mathbf{Me}_{12}(\mathrm{OH})_2$ is ionized (d) and reduced by electron attachment (e). Iso-surfaces are taken at ± 5e-3Å^{-3} and ± 2.5e-3Å^{-3} for ionization and electron attachment, with red indicating a reduction in electron density and blue indicating an increase. (f) Clipped electron density change iso-surface upon ionization taken at ± 5e-3Å^{-3}. (g,h) Clipped electron attachment density taken at ± 2.5e-3Å^{-3}. Notice the difference between belt and cap tin atoms (g) and the attachment density near the 5-coordinate belt tin atoms that resembles the Sn $5dz^2$ orbital (h).

We also report notable changes in cage geometry upon ionization. Consistent with previous calculations, a particular cap tin-carbon bond is weakened spontaneously and the associated methyl group relaxes into an sp^2 geometry as shown in figures 2 and S1. The drastic reduction in bond energy and change in methyl geometry is consistent with multi-reference calculations performed on ionized $Sn(CH_3)_3OH$.[39] Atomic displacements subsequent to ionization are magnified by 10 times and shown in red arrows in the bottom left panel of figure 2. The involved tin atom moves towards the center and is co-planar with the surrounding oxygen atoms. On the far left of the lower left panel of figure 2, we report the absence of significant atomic displacements upon removal of a cap methyl from an ionized cage. However, if a belt methyl group is removed from an ionized cage, the now 4-coordinate tin atom moves towards the center as the internal axial oxygen atom is drawn to this tin atom, indicating that a coordination number of 5 is significantly more stable than 4 in this system when it is ionized. This rearrangement appears to paint a picture where the hole migrates to the 4-coordinate tin atom, prompting it to relax by finding a fifth electron rich bonding neighbor.

Upon electron attachment, as one can see in the upper panel in figure 2, the bond strengths are reduced to 0.61 eV for cap and -0.12 eV for belt methyl groups as shown in figure 2. On top of the previously reported preferential destabilization of the belt tin-carbon bonds,[19] we discovered that the entropic contribution suffices to reduce the reaction free energy, resulting in a spontaneous entropy driven $CH_3^\bullet$ elimination at room temperature. Interestingly, compared to results using PBE0 functional at 0 K, our method and conditions (revPBE0-D3BJ/293K) actually result in a less exothermic reaction *enthalpy* (free energy minus entropy) of 0.115 eV. This could be attributed to the attractive dispersion interaction between the two fragments.

Also as a result of electron attachment, the radius of the belt increases negligibly and the cap to cap distance reduces slightly, as shown in the lower right panel in figure 2, resulting in an estimated marginal volume reduction of 1%. Given the molecule size and abundance of

electrons, atomic displacements are expected to be small. By amplifying them by 50 times, as illustrated in the bottom right panel of figure 2, we reveal that the oxygen atoms between the belt and cap are moving radially outward, opening up what appears to be the "sixth coordination site" and bringing the belt tin atoms closer to a "half octahedron" coordination. The cap tin and oxygen atoms are drawn simultaneously closer to the center. Such geometric changes seem to suggest that the extra electron resides, as shown in later discussions, around the belt tin atoms opposite to the methyl carbon.

Subsequent to tin-carbon bond cleavage, as shown in the far right column in 2, the involved tin atom moves away from the cage, indicating that the lone pair of the now full-shell cage is localized at the tin atom.

Another possible result of electron attachment is the ionic dissociation of the hydroxide anion. However, the dissociation free energy of the counter anion is 3.743 eV which is still on the order of a few eVs. In comparison, tin-cabon bond cleavage is a more likely outcome. The high counter anion dissociation energy barrier does not explain the correlation between resist performance and anion mass reported.[6] As we will discuss later on, there is a proton transfer mechanism involved to account for the presence of diffusing conjugate acid of the anions.

Elimination of CH_3^+ upon ionization is still less favorable than eliminating $CH_3^{\bullet}$. Elimination of CH_3^+ at the caps is only 0.04 eV more favorable than on the belt, which is consistent with computations for an un-ionized cage.

As mentioned, ionization and electron attachment selectively destabilize different tin-carbon bonds. This selectivity can be elucidated with the change in electron density subsequent to ionization or electron attachment. The iso-surfaces of electron density difference upon ionization and electron attachment is shown in figure 3(d) and (e). The vertical density changes, where atomic movements upon ionization or electron attachment are neglected, are shown.

Upon ionization, electron density mainly withdraws from between the tin and carbon

atoms surrounding the cap. For clarity, figure 3(d) is clipped to emphasize the cap methyl groups (figure 3(f)). Apparently, electron density is withdrawn from the bond into associated carbon atoms. Since the withdrawn density is located near the mid point of the tin-carbon bonds, it is bonding in nature. The diminished bonding density in cap tin-carbon bonds thus explains why it is preferentially destabilized. The withdrawal of density also explains the geometrical change previously shown in figure 2. The change in electron density correlates very well with the HOMO density (figure 3(b)).

Upon electron attachment, the overall change in electron density (figure 3(e)) is more nuanced. Regardless of the location, the electron density increases and decreases alternately along the length of the bond. The magnitude of modulation is very similar between cap and belt methyl groups. Interestingly, the carbon atom is actually located at a node between positive and negative electron density change. We produce a clipped cutout of figure 3(e) to closely examine the differences between cap and belt tin-carbon bonds in figure 3(g). Near the vertical center line are two belt tin-carbon bonds (enclosed by electron density iso-surfaces). Approximately 60 degrees counter clockwise from the them are two cap tin-carbon bonds. As one can see, there is extra electron density in the shape of a plug on the inside of the belt tin atoms. Such density, as shown in another cutout containing only belt tin atoms (figure 3(h)), is present underneath all belt Sn atoms, increasing electrostatic repulsion along the bond. The absence of such density in cap Sn atoms explains the relative destabilization of belt tin-carbon bonds and the geometrical change upon electron attachment shown in the bottom right panel of figure 2. Such "in-cage" density is also present in the LUMO orbital.

The plug like shape of the "in-cage" density partially resembles the $5dz^2$ orbitals of the tin atom, suggesting that their availability is key to its susceptibility to electron attachment. The tin atoms on the cap are 6-coordinate and the $5dz^2$ orbital is involved in bonding. The belt tin atoms are 5-coordinate and that explains the availability of empty $5dz^2$ orbitals. With this observation, we can generalize that in a complex tin-oxo system where tin atoms with different coordinate numbers co-exist, electron attachment density would concentrate around

14

the lowest-coordinate tin atom. From the observed locality of this phenomenon, whether the tin-oxo cage arranges itself into a cage is not expected to play a big role, suggesting that it would occur in similar clusters or even amorphous organic tin-oxo networks.

3.3 Ionic dissociation

Photoresists are condensed films and the environment can affect the coordination between the anions and the cage. The extent of these effects depends on how much the chemistry is affected by the anions.

To proceed, we investigate the consequences of removing the counter anion. We begin with the scenario where both anions are removed. In this case the inversion symmetry of the molecules is preserved so all belt and cap methyl groups are geometrically equivalent. The total ionic dissociation energy in vacuum is found to be 14.27 eV See figure S2.

Comparing bond energies in figures 2 and S3b, prior to electron addition and removal, the elimination of counter anions changes the $CH_3^{\bullet}$ elimination BDFE of the tin carbon bond by less than 0.1 eV. However, the absence of counter anions significantly increases the electrostatic energy of the system. As a result, the CH_3^{+} elimination BDFE sees a significant reduction of around 5 eV (figureS3b).

The bare cage (as illustrated in figure S3a) with a charge of 2+, has a ionization potential of 12.6 eV, which is much higher than 7.314 eV when both anions are present (see figure 2), and that agrees with experimentally measured fragmentation yield onset.[22] Subsequent to ionization, cap $CH_3^{\bullet}$ elimination BDFE is reduced by 2 eV to 0.24 eV. The process is not spontaneous. Yet the small barrier size implies that if the molecule is promoted to a low lying excited state, the process would likely be spontaneous. From experimental data, we see a steep rise less than a eV above the onset.[22] Elimination of CH_3^{+}, which is sensitive to Coulomb interaction, is exothermic once the bare cage is ionized to a charge of 3+. The presence of dealkylated cage with charge 3+ reported is therefore intriguing.[22] Multi-reference calculations on $Sn(CH_3)_3OH$ suggested the presence of multiple dissociative excited

15

state potential energy surfaces,[39] which could explain the observation.

With an extra electron, elimination of $CH_3^{\bullet}$ becomes spontaneous, just as when both the anions are present. The electron affinity of 5.943 eV is much higher in the absence of anions (1.122 eV). This is presumably a result of electrostatic interaction.

For $CH_3^{\bullet}$ elimination alone, the bond energies and excitation selectivity are similar with or without the anions. Noticeably though, the post-ionization bias towards cap methyl groups increases in the absence of anions. On the other hand, the post-attachment bias towards belt methyl groups decreases. Moreover, regardless of the absolute energies, post-ionization CH_3^{+} elimination is more belt-biased compared to post-ionization $CH_3^{\bullet}$ elimination, consistent with what is observed in the presence of both anions. It indicates that the orbital geometry arguments appears to be true regardless of the presence of counter anions.

Upon the removal of a single hydroxide counter anion, the inversion symmetry of the molecule is broken and there are two geometrically nonequivalent types of belt and cap groups as shown in figure S4. Cap-1 are those next to the empty anion site and the cap-2 are next to the remaining hydroxide anion, as illustrated in figure S4b and S4c. To understand the symmetry of belt groups, we take an axial view through which the two anion sites align. The cap-1 and cap-2 tin atoms (magenta and cyan) form two equilateral triangles that are a 60 degree azimuthal rotation apart. Belt tin-carbon bonds that azimuthally align with cap-1 groups are belt-1 groups (figure S4d). Similarly, belt tin-carbon bonds that share "longitudes" with cap-2 groups are belt-2 groups (figure S4e).

The BDFEs for $CH_3^{\bullet}$ elimination, as shown in figure S5, are similar to that with none or both of the hydroxide ions. $CH_3^{\bullet}$ elimination is still more likely to happen than CH_3^{+} elimination upon ionization or electron attachment.

Noticeably, cap-1 and cap-2 react very differently to ionization (figure S5b). Cap-2 tin-carbon bonds are weakened more than their cap-1 counterparts. Still, their BDFE (0.49 eV) is higher than when the cage has both (0.096 eV) or none (0.236 eV) of the hydroxide anions. To understand this behavior, we examine the canonical orbitals and we observe that the spin

density is not coming from the frontier orbitals. In fact, it is concentrated on the remaining hydroxide group (specifically in an oxygen p orbital) even though the near-degenerate HOMO and HOMO-1 are rather delocalized, as they are in the presence of both anions (figure 3). This unexpected location of the spin density points to strong non-Afbau behavior which has been reported in complex systems as a possible radical-stabilization mechanism.[42–44] With inversion symmetry broken, electron density moves towards the remaining hydroxide as a reaction to the localized hole, in the process shielding the alkyl groups from the hole and stabilizing the cap-2 tin-carbon bonds. As a result, although cap-2 bonds are still the most vulnerable, their bond strength is stronger compared with their center-symmetric relatives (with two or zero anions).

Moreover, upon electron attachment all tin-carbon bonds, with the exception of those close to the remaining hydroxide group (cap-2), are prone to spontaneous cleavage.

3.4   Tin-Carbon Thermal Chemistry

From the trends observed in BDFEs under various circumstances, the geometries of frontier orbitals appear to explain much of the thermal-chemistry, including the excitation selectivity and the tilt in bond cleavage preference in CH_3^+ elimination. This is consistent with previous reports. Our investigation revealed that either impact ionization or electron attachment alone can result in cleavage and the two processes need not converge. In other words, one ionization-electron pair could lead to two useful chemical events. This gives organotin systems an edge over CAR systems. As mentioned previously, acid generation in CARs is still a research problem. Yet, according to the leading hypotheses, ionization and electron attachment induced chemistry need to rendezvous for acid generation.[9,12] As a result, one ionization-electron pair can likely generate only one acid.

The belt (5-coordinate) and cap (6-coordinate) tin atoms are sensitive to different chemical triggers, a behavior largely explained by frontier-orbital geometries and charge-density distribution. As the orbitals are non-local in nature, it begs the question whether juxtapos-

ing two types of tin atoms contributed to the sensitivity. In other words, if one is to make a hypothetical tin cluster consisting of only 5- or 6-coordinate tin, would the reactivity or sensitivity decrease? Recent experiments indicate that sensitivity, albeit to a lesser extent, can be achieved by the $\mathbf{Sn}_6$ "drum" cluster, which is comprised of only 6-coordinate tin atoms,[8] suggesting that such juxtaposition is not necessary for lithographic sensitivity. However, "football" cluster is still faster than the "drum" in e-beam lithography and that appears to support the advantage of having both 5- and 6- coordinate tin atoms.

That study raised two interesting points. Firstly, it suggested that counter anion dissociation plays a bigger role than tin-carbon bond cleavage. However, acetic acid out-gassing from the "football" cluster is similar to the "drum" cluster after normalizing for the tin-to-acetate ratio. The "drum" has one tin atom per acetate whereas the "football" has six. The acetic acid yield of the "drum" is around 4 to 8 times that of the "football", which is consistent with the tin-to-acetate ratio, suggesting that the "football" cluster is not better at producing acetic acid than the "drum" cluster.

Secondly, out gassing of acetic acid, which is the conjugate acid of the counter anion, was reported. Yet our computations have yet to provide explanations for the very existence of conjugate acids. On top of that, there is an indisputably clear link between counter anion mass and sensitivity.[6] The reported benefits of post exposure bake[24] are also consistent with the notion that diffusion is an integral part of the exposure chemistry. In light of those results, it is almost certain that there exists a pathway for protons to recombine with the anions, resulting in the conjugate acid. Given that ionization-induced deprotonation is a widely studied subject in chemically amplified resists, we investigated whether a similar phenomenon takes place in the $[(R-Sn)_{12}O_{14}(OH)_6](A)_2$ family.

3.5 Proton transfer

Upon ionization, hole transfer and eventual deprotonation have been investigated and reported to play an integral role in acid generation in EUV chemically amplified resists.[12,45] In

$\mathbf{Sn_{12}Me_{12}(OH)_x}$, surprisingly, we report the auto deprotonation of terminal hydroxyl groups attached cap tin atoms in the presence of one or two hydroxide counter anions. In the process of geometric relaxation, a hydrogen atom detaches from the cap of the cage and combines with a hydroxide counter anion, essentially neutralizing the hydroxide base.

Deprotonation is slightly different depending on the number of counter anions. With two hydroxide anions, deprotonation occurs as a result of ionization. In the presence of a single anion, ionization does not result in deprotonation. However, a combination of ionization and dealkylation of the belt or cap-2 alkyl groups does trigger deprotonation.

Deprotonation does not occur in the absence of counter anions. We anticipate similar behavior when the anion is a strong base and, which by definition, has a weak conjugate acid, and that is the case in a previous study.[6] In that study, a larger counter anion is shown to reduce dose-to-clear, hinting at the role of diffusion of the counter anions. However, the anions are bonded by Coulomb interaction to the cap of the cages, making diffusion inherently difficult at room temperature. Our observation presents a channel for the conjugate base to be neutralized, providing an explanation for the linearity between anion size and dose-to-clear.

To examine this hypothesis, we compared the energetics of a few different bases, including the aforementioned hydroxide (A$^-$ = OH$^-$ pKa $\sim$ 14 in water[46,47]), formate (A$^-$ = CHO$_2^-$ pKa $\sim$ 4 in water), and methanesulfonate (A$^-$ = CH$_3$SO$_3^-$ pKa $\sim$ -1 in water). These are common counter anions for this system. Sulfonate and hydroxide anions are the weakest and strongest conjugate bases. Most counter anions are carboxylates for which formate is an archetypal representative . Given the size of the methanesulfonate group, Hessian calculations were omitted and energy differences reported are electronic self-consistent energy evaluated at revPBE0-D3BJ/def2-TZVP on geometries optimized at revPBE0-D3BJ/def2-SVP.

The relaxed structures are shown in figure 4. In the presence of hydroxide anion, deprotonation occurs spontaneously upon ionization—a stable geometry with two hydroxide anions does not exist. We started the geometric minimization with two anions but depro-
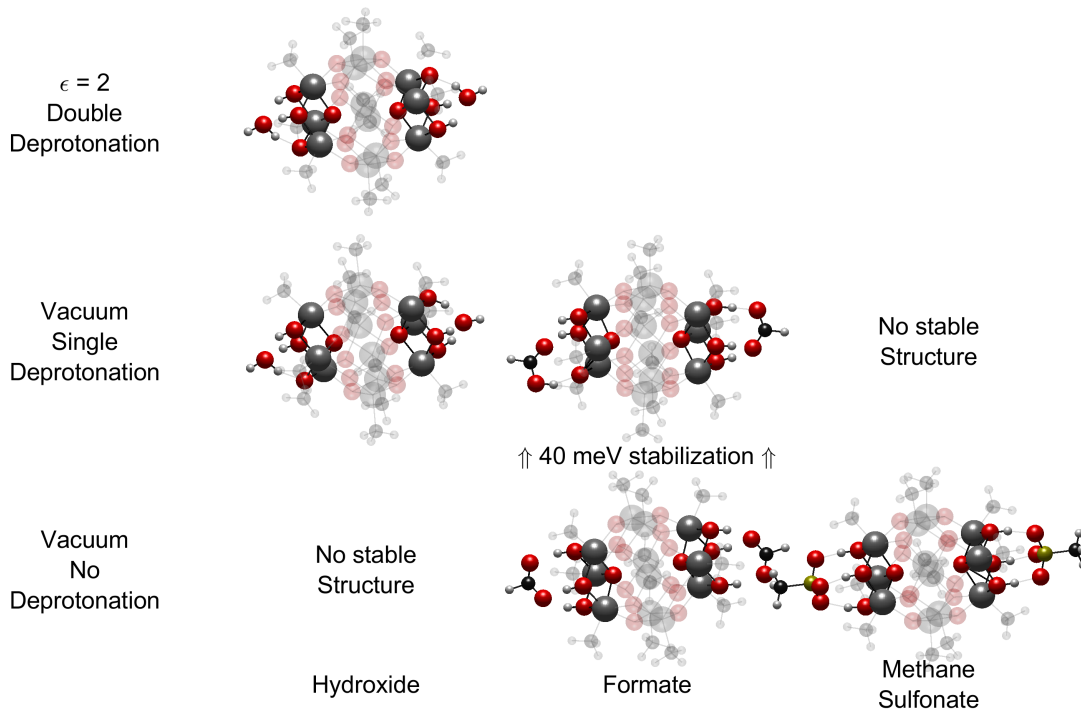
Figure 4: The structures of $\mathbf{Sn}_{12}\mathbf{Me}_{12}A_2$ clusters at various degrees of cage deprotonation. Red, gray, black, white, and yellow atoms are oxygen, tin, carbon, hydrogen, and sulfur, respectively. The anions (A^-) hydroxide (OH^-), formate (CHO_2^-), and methanesulfonate ($CH_3SO_3^-$) are considered. The crown-like structure at the caps and the anions are highlighted for clarity

tonation proceeds spontaneously in geometric relaxation. With the formate anion (center column in figure 4), stable geometries exist with or without deprotonation and the deprotonated geometry is around 40 meV more stable than its bi-anion counterpart. In other words, at room temperature, even with the precision of our calculations accounted for, a significant portion of ionized formate cluster would deprotonate and produce formic acid molecules. Moreover, the existence of stable geometries for both deprotonated and protonated $[\mathbf{Sn}_{12}\mathbf{Me}_{12}(CHO_2^-)_2]^+$ indicates the presence of an energy barrier for deprotonation. Whether this is a correlation between the barrier height and basicity could be an interesting question. Noticeably, formic acid is a rather acidic member of the carboxylic acid family, the

common choice for counter anion for $[\mathbf{Sn_{12}Me_{12}}]^{2+}(A^-)_2$ systems.[6,24] Thus, the propensity of formate anion to deprotonate the cage suggests that it would be a common occurrence in most carboxylic acids, providing an explanation for the anion mass dependence of resist sensitivity. Lastly, we could not observe any stable deprotonated geometry when methane-sulfonate ($A^- = CH_3SO_3^-$) is used as the counter anion—even when a deprotonated initial geometry is used, the methanesulfonic acid spontaneously dissociates and re-protonates the cage.

We anticipate ionization-induced deprotonation to be more prevalent in condensed phase resist, as the dielectric background is likely to substantially affect proton-transfer energy. By raising the dielectric constant from 1 (vacuum) to 2 both hydroxide ions in $[\mathbf{Sn_{12}Me_{12}}]^{2+}(OH^-)_2$ are predicted to be neutralized by cage deprotonation (Top left of figure 4). This suggests that vacuum computations are underestimating the likelihood of deprotonation and thus providing a conservative estimate of the degree of proton transfer from cage to anions.

The presented ionization-driven acid generation has a few implications on our under-standing of these materials, as an EUV resist and beyond. Spatial propagation of chemistry in these materials has been assumed to be minimal, at least in modeling studies.[48] Our computations, consistent with experiments,[6] suggest the presence of thermally-mobile acid upon ionization. Without initiating any reaction, the diffusion of acid away from the ex-posed volumes would facilitate condensation (or formation of chemical bonds), resulting in lower dose. It has been reported that lighter counter anions and higher post-exposure bake temperatures result in higher sensitivity.[24] Our computations have provided another piece of evidence along this line of reasoning. Such diffusion is likely to have an impact on the line-edge-roughness (LER) of the resist as in chemically amplified resists.[11]

Utilizing the acid as a reagent of the exposure chemistry would however be challeng-ing. In existing synthetic schemes, the conjugate acids of the counter anions are used as a reagent.[24,30] In the process, $[\mathbf{Sn_{12}Me_{12}}]^{2+}(A^-)_2$ is exposed to its conjugate acid, suggest-ing that the cage and tin-carbon bonds are inert to the conjugate acid. However, since

$[\mathbf{Sn}_{12}\mathbf{Me}_{12}]^{2+}(\mathrm{A}^-)_2$ can be separated into solid powders, it is conceivable to include acid-labile components into the formulation.
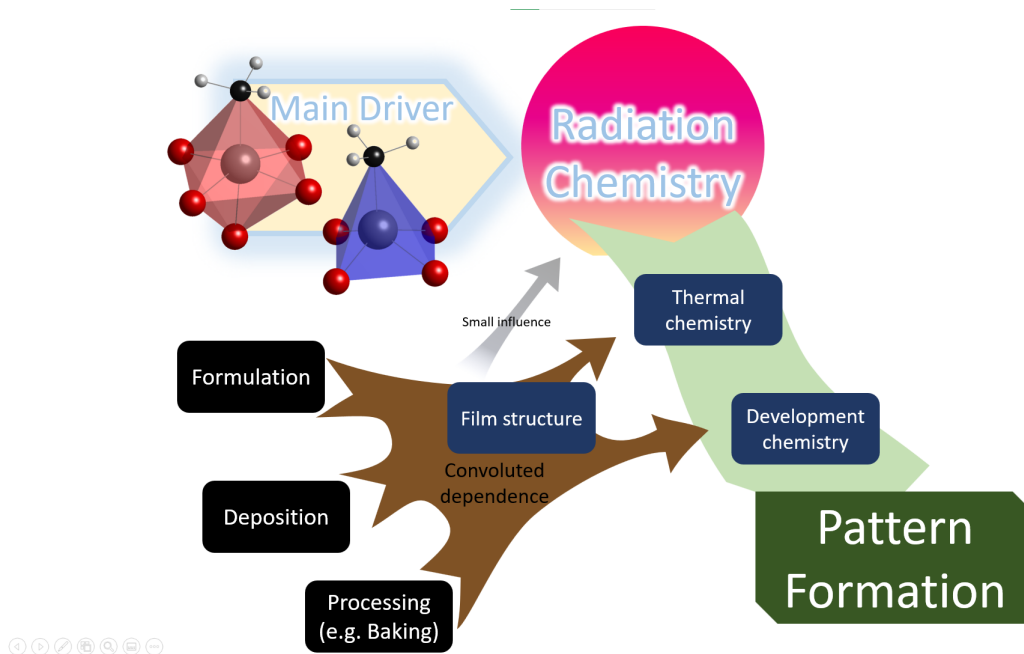
4 Conclusion

Figure 5: Summary—The radiation chemistry can be largely explained by electron density changes localized to the tin atoms. As a result, radiation chemistry can be decoupled from other factors such as formulation and processing, eventually simplifying the material identification problem.

With our systematic study of the $[\mathbf{Sn}_{12}\mathbf{Me}_{12}]^{2+}(\mathrm{A}^-)_2$ system, we have further upheld the understanding that cleavage of tin-carbon bonds dominates the chemistry of this system. Our computations have provided a molecular-level understanding of the sensitization mechanism, illustrating that either ionization or electron attachment can trigger tin-carbon bond cleavage. As mentioned in section 3.4, such full utilization of the electron–hole pair generated by each impact ionization event could explain the superiority of tin-oxo resists for EUV applications. The ability to initiate chemistry with both impact ionization and electron attachment is a stark contrast to chemically amplified systems (CAR), the incumbent workhorse adopted from DUV lithography. In CARs, impact ionization and electron

attachment induced chemistry is understood to converge in order to produce an acid.[9,12] As a result, an electron-ionization pair can at most create one acid in CARs. In contrast, an electron-ionization pair can create two active sites in the resist film, practically doubling the quantum efficiency, which is vital in combating the RLS trade-off.[10,11]

Moreover, while how ionization and electron attachment initiate chemistry in this organotin-oxo system has been elucidated, there are still considerable unknowns regarding how ionization and electron attachment lead to acid generation in EUV CAR systems. These uncertainties are related to the fact that CAR systems are adapted from DUV. Engineers have to treat acid generation more or less as a black box and that hinders rational design. This highlights the advantage of material platforms conceived specifically for EUV lithography— their EUV specific chemistry gives cleaner mechanisms, which in turn makes rational design more viable.

On top of predicting an excitation selectivity as previously reported, we have demonstrated that selectivity is generally not affected by the presence of anions. Such robustness in this selectivity would set the stage for possible selectivity engineering in the future—by placing different side chains on tin atoms on the belt and the cap, one can generate different chemical outcomes subsequent to ionization and electron attachment.

A further investigation into the origin of such selectivity also suggests that the large "in-cage" LUMO and vertical attachment density located at 5-coordinate (belt) tin atoms contributes to this selectivity. Such density is rather localized and resembles a dz^2 orbital, suggesting that the chemical environment beyond the coordinating oxygen and carbon would do little to its electron affinity. Similarly, the HOMO is localized to the tin-carbon bonds at the caps, thus explaining their sensitivity to impact ionization. These observations could therefore be valid for other tin-oxo system regardless of the exact geometry, or in other words, the arrangements of tin tetrahedrons.

In the broader context, this discovery can speed up EUV material development. Resist chemistry has generally been very convoluted. As shown in figure 5, the radiation chem-

istry only initiates the pattern formation and there are various processes that lie between. Generally speaking, these processes, together with radiation chemistry, have complicated dependence with tuning parameters such as formulation, deposition, and additional processing such as baking. Such interdependence increases the difficulty in targeted material design as one can hardly disentangle them. In our study, we demonstrated that the radiation chemistry efficiency is related to the immediate coordination of the tin-carbon bond. As a result, as long as the local coordination is preserved, one can expect the efficacy of radiation chemistry to remain similar upon changes in formulation, processing, or even macro-molecular structure as illustrated previous studies.[8]

On top of tin-carbon cleavage, the relevance of anion conjugate acid has been reported.[6,8] Our computation has illustrated that ionization–deprotonation is a possible explanation of such acids, providing a starting point for creating formulations around this reaction route. Its propensity can be modulated by the basicity of counter anion. Since this deprotonation has been shown to be favorable with carboxylate ions common in $[\mathbf{Sn}_{12}\mathbf{Me}_{12}]^{2+}(\mathrm{A}^-)_2$ systems, we propose that such exposure-induced acid can be factored into resist formulation.

Our computations ultimately shed light on the dissolution chemistry. Methyl elimination opens sites for hydroxyl substitution,[21] a process conceivably facilitated by water in the environment or in the material itself. This could ultimately lead to condensation cross-linking reaction reported in hafnium based systems[5] and this is also consistent with the observation that this material is negative tone.[24] The evolution of anion conjugate acid would facilitate contact of neighboring organotin-oxo cages, enhancing the said condensation process. Both processes can be sped up with heat. Therefore upon exposure, the material loses aliphatic moieties, loses ionic character, and grows in molecular weight, all of which would lead to solubility changes.

The environment, particularly moisture, could play a role. Water would facilitate hydroxyl substitution mentioned above and, as shown in section 3.5, enhance the elimination of anion conjugate acid by increasing the material's dielectric constant. Therefore, moisture,

if managed properly, can potentially be a useful "knob" for tuning.

Supporting Information

The effect of ionization on the geometry of $\mathbf{Sn_{12}Me_{12}(OH)_2}$ is highlighted in figure S1. The ionic dissociation energies of $\mathbf{Sn_{12}Me_{12}(OH)_2}$ are shown in S2. A free energy diagram of methyl (radical and cation) elimination from $[\mathbf{Sn_{12}Me_{12}}]^{2+}$, and its ionization and electron attachment products, is shown in figure S3. Figure S4 is a graphical guide for locating cap-1, cap-2, belt-1, and belt-2 groups in $[\mathbf{Sn_{12}Me_{12}OH}]^{+}$. Finally, the free energy diagram of methyl (radical and cation) elimination from $[\mathbf{Sn_{12}Me_{12}OH}]^{+}$, and its ionization and electron attachment products, is shown in figure S5.

Acknowledgement

References

(1) Lv, H.; Geletii, Y. V.; Zhao, C.; Vickers, J. W.; Zhu, G.; Luo, Z.; Song, J.; Lian, T.; Musaev, D. G.; Hill, C. L. Polyoxometalate Water Oxidation Catalysts and the Production of Green Fuel. *Chem. Soc. Rev.* **2012**, *41*, 7572–7589.

(2) Liu, J.-X.; Gao, M.-Y.; Fang, W.-H.; Zhang, L.; Zhang, J. Bandgap Engineering of Titanium–Oxo Clusters: Labile Surface Sites Used for Ligand Substitution and Metal Incorporation. *Angewandte Chemie International Edition* **2016**, *55*, 5160–5165.

(3) Judd, D. A.; Nettles, J. H.; Nevins, N.; Snyder, J. P.; Liotta, D. C.; Tang, J.; Ermolieff, J.; Schinazi, R. F.; Hill, C. L. Polyoxometalate HIV-1 Protease Inhibitors. A New Mode of Protease Inhibition. *Journal of the American Chemical Society* **2001**, *123*, 886–897, PMID: 11456622.

(4) Durand, S.; Sakamoto, K.; Fukuyama, T.; Orita, A.; Otera, J.; Duthie, A.; Dakternieks, D.; Schulte, M.; Jurkschat, K. Cationic Organotin Clusters for Highly Efficient Alcohol Acetylation Catalysts. *Organometallics* **2000**, *19*, 3220–3223.

(5) Stowers, J. K.; Telecky, A.; Kocsis, M.; Clark, B. L.; Keszler, D. A.; Grenville, A.; Anderson, C. N.; Naulleau, P. P. Directly Patterned Inorganic Hardmask for EUV Lithography. *Extreme Ultraviolet (EUV) Lithography II* **2011**, *796915*, 796915.

(6) Cardineau, B.; Del Re, R.; Marnell, M.; Al-Mashat, H.; Vockenhuber, M.; Ekinci, Y.; Sarma, C.; Freedman, D. A.; Brainard, R. L. Photolithographic Properties of Tin-Oxo Clusters Using Extreme Ultraviolet Light (13.5nm). *Microelectronic Engineering* **2014**, *127*, 44 – 50.

(7) Re, R. D.; Passarelli, J.; Sortland, M.; Cardineau, B.; Ekinci, Y.; Buitrago, E.; Neisser, M.; Freedman, D. A.; Brainard, R. L. Low-Line Edge Roughness Extreme Ultraviolet Photoresists of Organotin Carboxylates. *Journal of Micro/Nanolithography, MEMS, and MOEMS* **2015**, *14*, 1 – 7.

(8) Sharps, M.; Frederick, R.; Javitz, M.; Herman, G.; Johnson, D.; Hutchison, J. Organotin Carboxylate Reagents for Nanopatterning: Chemical Transformations During Direct-Write Electron Beam Processes. *Chemistry of Materials* **2019**, *31*, 4840–4850.

(9) Wallraff, G. M.; Hinsberg, W. D. Lithographic Resists. *Encyclopedia of Polymer Science and Technology* **2002**, *6*, 660–696.

(10) Gallatin, G. M.; Naulleau, P.; Brainard, R. Fundamental Limits to EUV Photoresist. Advances in Resist Materials and Processing Technology XXIV. 2007; pp 387 – 396.

(11) Naulleau, P.; Gallatin, G. Relative Importance of Various Stochastic Terms and EUV Patterning. *Journal of Micro/Nanolithography, MEMS, and MOEMS* **2018**, *17*, 1 – 7.

(12) Kozawa, T.; Tagawa, S. Radiation Chemistry in Chemically Amplified Resists. *Japanese Journal of Applied Physics* **2010**, *49*.

(13) Ogletree, D. F. In *Materials and Processes for Next Generation Lithography*; Robinson, A., Lawson, R., Eds.; Frontiers of Nanoscience; Elsevier, 2016; Vol. 11; pp 91 – 113.

(14) Banse, F.; Ribot, F.; Toledano, P.; Maquet, J.; Sanchez, C. Hydrolysis of Monobutyltin Trialkoxides: Synthesis and Characterizations of (BuSn)12O14(OH)6(OH)2. *Inorganic Chemistry* **1995**, *34*, 6371–6379.

(15) Henke, B.; Gullikson, E.; Davis, J. X-Ray Interactions: Photoabsorption, Scattering, Transmission, and Reflection at E = 50-30,000 eV, Z = 1-92. *Atomic Data and Nuclear Data Tables* **1993**, *54*, 181–342.

(16) Anderson, C.; Allezy, A.; Chao, W.; Conley, L.; Cork, C.; Cork, W.; Delano, R.; DePonte, J.; Dickinson, M.; Gaines, G.; Gamsby, J.; Gullikson, E.; Jones, G.; McQuade, L.; Miyakawa, R.; Naulleau, P.; Rekawa, S.; Salmassi, F.; Vollmer, B.; Zehm, D.;

Zhu, W. How We Are Making the 0.5-NA Berkeley Mirco-Field Exposure Tool Stable and Productive. Extreme Ultraviolet (EUV) Lithography XI. 2020; pp 48 – 55.

(17) Allenet, T. P.; Vockenhuber, M.; Yeh, C.-K.; Santaclara, J. G.; van Lent-Protasova, L.; Ekinci, Y. Progress in EUV Resist Screening by Interference Lithography for High-Na Lithography. International Conference on Extreme Ultraviolet Lithography 2021. 2021.

(18) Santaclara, J. G.; Rispens, G.; Bekaert, J.; Thiam, A.; Maslow, M.; Hoefnagels, R.; Zuurbier, N.; van Lent-Protasova, L.; Yin, F. C. Today's Scorecard for Tomorrow's Photoresist: Progress and Outlook Towards High-Na EUV Lithography. Advances in Patterning Materials and Processes XXXVIII. 2021.

(19) Ma, J. H.; Wang, H.; Prendergast, D.; Neureuther, A.; Naulleau, P. Excitation Selectivity in Model Tin-Oxo Resist: A Computational Chemistry Perspective. Extreme Ultraviolet (EUV) Lithography XI. 2020; pp 349 – 355.

(20) Bespalov, I.; Zhang, Y.; Haitjema, J.; Tromp, R.; Van Der Molen, S.; Brouwer, A.; Jobst, J.; Castellanos, S. Key Role of Very Low Energy Electrons in Tin-Based Molecular Resists for Extreme Ultraviolet Nanolithography. *ACS Applied Materials and Interfaces* **2020**, *12*, 9881–9889.

(21) Haitjema, J.; Zhang, Y.; Ottosson, N.; Brouwer, A. Photoreactions of Tin Oxo Cages, Model EUV Photoresists. *Journal of Photopolymer Science and Technology* **2017**, *30*, 99–102.

(22) Haitjema, J.; Wu, L.; Giuliani, A.; Nahon, L.; Castellanos, S.; Brouwer, A. Photo-Induced Fragmentation of a Tin-Oxo Cage Compound. *Journal of Photopolymer Science and Technology* **2018**, *31*, 243–247.

(23) Zhang, Y.; Haitjema, J.; Liu, X.; Johansson, F.; Lindblad, A.; Castellanos, S.; Ottosson, N.; Brouwer, A. Photochemical Conversion of Tin-Oxo Cage Compounds Studied

Using Hard X-Ray Photoelectron Spectroscopy. *Journal of Micro/ Nanolithography, MEMS, and MOEMS* **2017**, *16*.

(24) Haitjema, J.; Zhang, Y.; Vockenhuber, M.; Kazazis, D.; Ekinci, Y.; Brouwer, A. Extreme Ultraviolet Patterning of Tin-Oxo Cages. 2017.

(25) Hutchison, D.; Stern, R.; Olsen, M.; Zakharov, L.; Persson, K.; Nyman, M. Alkyltin Clusters: The Less Symmetric Keggin Isomers. *Dalton Transactions* **2018**, *47*, 9804–9813.

(26) Zhu, Y.; Olsen, M.; Nyman, M.; Zhang, L.; Zhang, J. Stabilizing γ-Alkyltin-Oxo Keggin Ions by Borate Functionalization. *Inorganic Chemistry* **2019**, *58*, 4534–4539.

(27) Stern, R. D.; Hutchison, D. C.; Olsen, M. R.; Zakharov, L. N.; Nyman, M.; Persson, K. A. Alkyltin Keggin Clusters as EUVL Photoresist Technology. International Conference on Extreme Ultraviolet Lithography 2019. 2019; pp 181 – 188.

(28) Day, V. W.; Eberspacher, T. A.; Klemperer, W. G.; Park, C. W. Dodecatitanates: A New Family of Stable Polyoxotitanates. *Journal of the American Chemical Society* **1993**, *115*, 8469–8470.

(29) Müller, A.; Rohlfing, R.; Krickemeyer, E.; Bögge, H. Control of the Linkage of Inorganic Fragments of v-O Compounds: From Cluster Shells as Carcerands via Cluster Aggregates to Solid-State Structures. *Angewandte Chemie International Edition in English* **1993**, *32*, 909–912.

(30) Eychenne-Baron, C.; Ribot, F.; Sanchez, C. New Synthesis of the Nanobuilding Block (BuSn)12O14(OH)62+and Exchange Properties of (BuSn)12O14(OH)6(O3SC6H4CH3)2. *Journal of Organometallic Chemistry* **1998**, *567*, 137 – 142.

(31) Puff, H.; Reuter, H. Zur Hydrolyse Von Monoorganylzinn-Trihalogeniden III. Isolierung Und Röntgenstrukturanalyse Von Verbindungen Mit Dem Neuartigen Käfig-Ion [(I-PrSn)12O14(OH)6]2+. *Journal of Organometallic Chemistry* **1989**, *373*, 173 – 184.

(32) Plasseraud, L.; Cattey, H.; Richard, P. [(PhCH2Sn)12(μ3-O)14(μ-OH)6](F3CSO3)2: A New Dodecanuclear Organostannoxane. *Zeitschrift Für Naturforschung B* **01 Mar. 2011**, *66*, 262 – 268.

(33) Zhang, Y.; Yang, W. Comment on "Generalized Gradient Approximation Made Simple". *Phys. Rev. Lett.* **1998**, *80*, 890–890.

(34) Perdew, J. P.; Ernzerhof, M.; Burke, K.; Perdew, J. P.; Ernzerhof, M.; Burke, K. Rationale for Mixing Exact Exchange With Density Functional Approximations Rationale for Mixing Exact Exchange With Density Functional Approximations. **1996**, *22*, 9982–9985.

(35) Mardirossian, N.; Head-Gordon, M. Thirty Years of Density Functional Theory in Computational Chemistry: An Overview and Extensive Assessment of 200 Density Functionals. *Molecular Physics* **2017**, *115*, 2315–2372.

(36) Grimme, S.; Antony, J.; Ehrlich, S.; Krieg, H. A Consistent and Accurate Ab Initio Parametrization of Density Functional Dispersion Correction (DFT-D) for the 94 Elements H-Pu. *The Journal of Chemical Physics* **2010**, *132*, 154104.

(37) Grimme, S.; Ehrlich, S.; Goerigk, L. Effect of the Damping Function in Dispersion Corrected Density Functional Theory. *Journal of Computational Chemistry* **2011**, *32*, 1456–1465.

(38) Shao, Y.; Gan, Z.; Epifanovsky, E.; Gilbert, A. T.; Wormit, M.; Kussmann, J.; Lange, A. W.; Behn, A.; Deng, J.; Feng, X.; Ghosh, D.; Goldey, M.; Horn, P. R.; Jacobson, L. D.; Kaliman, I.; Khaliullin, R. Z.; Kuś, T.; Landau, A.; Liu, J.; Proynov, E. I.;

Rhee, Y. M.; Richard, R. M.; Rohrdanz, M. A.; Steele, R. P.; Sundstrom, E. J.; III, H. L. W.; Zimmerman, P. M.; Zuev, D.; Albrecht, B.; Alguire, E.; Austin, B.; Beran, G. J. O.; Bernard, Y. A.; Berquist, E.; Brandhorst, K.; Bravaya, K. B.; Brown, S. T.; Casanova, D.; Chang, C.-M.; Chen, Y.; Chien, S. H.; Closser, K. D.; Crittenden, D. L.; Diedenhofen, M.; Jr., R. A. D.; Do, H.; Dutoi, A. D.; Edgar, R. G.; Fatehi, S.; Fusti-Molnar, L.; Ghysels, A.; Golubeva-Zadorozhnaya, A.; Gomes, J.; Hanson-Heine, M. W.; Harbach, P. H.; Hauser, A. W.; Hohenstein, E. G.; Holden, Z. C.; Jagau, T.-C.; Ji, H.; Kaduk, B.; Khistyaev, K.; Kim, J.; Kim, J.; King, R. A.; Klunzinger, P.; Kosenkov, D.; Kowalczyk, T.; Krauter, C. M.; Lao, K. U.; Laurent, A. D.; Lawler, K. V.; Levchenko, S. V.; Lin, C. Y.; Liu, F.; Livshits, E.; Lochan, R. C.; Luenser, A.; Manohar, P.; Manzer, S. F.; Mao, S.-P.; Mardirossian, N.; Marenich, A. V.; Maurer, S. A.; Mayhall, N. J.; Neuscamman, E.; Oana, C. M.; Olivares-Amaya, R.; O'Neill, D. P.; Parkhill, J. A.; Perrine, T. M.; Peverati, R.; Prociuk, A.; Rehn, D. R.; Rosta, E.; Russ, N. J.; Sharada, S. M.; Sharma, S.; Small, D. W.; Sodt, A.; Stein, T.; Stück, D.; Su, Y.-C.; Thom, A. J.; Tsuchimochi, T.; Vanovschi, V.; Vogt, L.; Vydrov, O.; Wang, T.; Watson, M. A.; Wenzel, J.; White, A.; Williams, C. F.; Yang, J.; Yeganeh, S.; Yost, S. R.; You, Z.-Q.; Zhang, I. Y.; Zhang, X.; Zhao, Y.; Brooks, B. R.; Chan, G. K.; Chipman, D. M.; Cramer, C. J.; III, W. A. G.; Gordon, M. S.; Hehre, W. J.; Klamt, A.; III, H. F. S.; Schmidt, M. W.; Sherrill, C. D.; Truhlar, D. G.; Warshel, A.; Xu, X.; Aspuru-Guzik, A.; Baer, R.; Bell, A. T.; Besley, N. A.; Chai, J.-D.; Dreuw, A.; Dunietz, B. D.; Furlani, T. R.; Gwaltney, S. R.; Hsu, C.-P.; Jung, Y.; Kong, J.; Lambrecht, D. S.; Liang, W.; Ochsenfeld, C.; Rassolov, V. A.; Slipchenko, L. V.; Subotnik, J. E.; Voorhis, T. V.; Herbert, J. M.; Krylov, A. I.; Gill, P. M.; Head-Gordon, M. Advances in Molecular Quantum Chemistry Contained in the Q-Chem 4 Program Package. *Molecular Physics* **2015**, *113*, 184–215.

(39) Chalabala, J.; Dvořák, O.; Slavíček, P. Ab Initio Photodynamics of Model EUV Photoresists. *Chemical Physics* **2018**, *515*, 221–230.

(40) Levine, D. S.; Hait, D.; Tubman, N. M.; Lehtola, S.; Whaley, K. B.; Head-Gordon, M. CASSCF With Extremely Large Active Spaces Using the Adaptive Sampling Configuration Interaction Method. *Journal of Chemical Theory and Computation* **2020**, *16*, 2340–2354, PMID: 32109055.

(41) Frederick, R.; Saha, S.; Trey Diulus, J.; Luo, F.; Amador, J.; Li, M.; Park, D.-H.; Garfunkel, E.; Keszler, D.; Herman, G. Thermal and Radiation Chemistry of Butyltin Oxo Hydroxo: A Model Inorganic Photoresist. *Microelectronic Engineering* **2019**, *205*, 26–31.

(42) Zuo, T.; Xu, L.; Beavers, C. M.; Olmstead, M. M.; Fu, W.; Crawford, T. D.; Balch, A. L.; Dorn, H. C. M2@C79N (M = Y, Tb): Isolation and Characterization of Stable Endohedral Metallofullerenes Exhibiting M-M Bonding Interactions Inside Aza[80]fullerene Cages. *Journal of the American Chemical Society* **2008**, *130*, 12992–12997, PMID: 18774804.

(43) Gryn'ova, G.; Coote, M. L.; Corminboeuf, C. Theory and Practice of Uncommon Molecular Electronic Configurations. *WIREs Computational Molecular Science* **2015**, *5*, 440–459.

(44) Kumar, A.; Sevilla, M. D. SOMO–HOMO Level Inversion in Biologically Important Radicals. *The Journal of Physical Chemistry B* **2018**, *122*, 98–105, PMID: 29240424.

(45) Yamamoto, H.; Kozawa, T.; Tagawa, S.; Cao, H. B.; Deng, H.; Leeson, M. J. Polymer-Structure Dependence of Acid Generation in Chemically Amplified Extreme Ultraviolet Resists. *Japanese Journal of Applied Physics* **2007**, *46*, L142–L144.

(46) Marshall, W. L.; Franck, E. U. Ion Product of Water Substance, 0-1000 °C, 1-10,000 Bars New International Formulation and Its Background. *Journal of Physical and Chemical Reference Data* **1981**, *10*, 295–304.

(47) Bandura, A. V.; Lvov, S. N. The Ionization Constant of Water Over Wide Ranges of Temperature and Density. *Journal of Physical and Chemical Reference Data* **2006**, *35*, 15–30.

(48) Hinsberg, W. D.; Meyers, S. A Numeric Model for the Imaging Mechanism of Metal Oxide EUV Resists. Advances in Patterning Materials and Processes XXXIV. 2017; pp 14 – 24.

Graphical TOC Entry